

Bilayer Quantum Hall States in an n-Type Wide Tellurium Quantum Well

Chang Niu, Gang Qiu, Yixiu Wang, Mengwei Si, Wenzhuo Wu, and Peide D. Ye*



Cite This: <https://doi.org/10.1021/acs.nanolett.1c01705>



Read Online

ACCESS |



Metrics & More



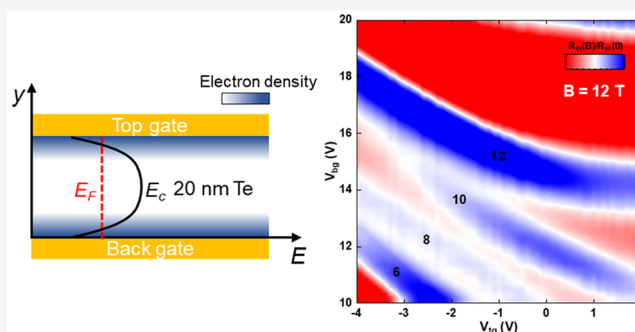
Article Recommendations



Supporting Information

ABSTRACT: Tellurium (Te) is a narrow bandgap semiconductor with a unique chiral crystal structure. The topological nature of electrons in the Te conduction band can be studied by realizing n-type doping using atomic layer deposition (ALD) technique on two-dimensional (2D) Te film. In this work, we fabricated and measured the double-gated n-type Te Hall-bar devices, which can operate as two separate or coupled electron layers controlled by the top gate and back gate. Profound Shubnikov–de Haas (SdH) oscillations are observed in both top and bottom electron layers. Landau level hybridization between two layers, compound and charge-transferable bilayer quantum Hall states at filling factor $\nu = 4, 6, \text{ and } 8$, are analyzed. Our work opens the door for the study of Weyl physics in coupled bilayer systems of 2D materials.

KEYWORDS: Tellurium, quantum Hall effect, bilayer system, Weyl Fermions



Bilayer systems that are made by confining electrons in two thin layers, exhibit a variety of phenomena, including integer and fractional quantum Hall effect,^{1–8} Hall drag,⁹ Coulomb drag,¹⁰ and exciton condensation.^{11–13} The structure-induced additional layer degree of freedom provides an ideal platform for the research on strongly correlated electrons and multicomponent physics.¹⁴ Compared to traditional double quantum wells based on GaAs and Al_xGa_{1–x}As,¹⁵ bilayer systems in wide quantum wells possess similar physics.^{2,16}

A bilayer electron system is realized in the tellurium (Te) wide quantum well structure with two different electrical field induced two-dimensional electron gases (2DEGs) at the top and bottom surface of the Te crystal as illustrated in Figure 1a. The nearly intrinsic Te between two conducting layers creates a potential barrier for the electron tunneling. By controlling the top and back gate bias and the magnetic field, electron density, tunneling interaction, interlayer, and intralayer Coulomb interaction can be tuned in a single device.

The crystal structure of right-handed trigonal Te is shown in Figure 1a. Covalently bonded Te atoms form a chiral atomic chain with three-fold screw symmetry along the *z*-axis. The helical chains are arranged in a trigonal lattice through van der Waals interaction. Te is a narrow band gap semiconductor. The conduction band minimum which contains two-fold valley and two-fold spin degeneracies is at the corner of the first Brillouin zone (*H* and *H'*).¹⁷ The unique crystal structure with chiral screw symmetry and the strong spin–orbit coupling of Te¹⁸ bring exotic physical properties, including the camelback band structure in the Te valence band,^{19,20} radial spin

texture,^{21–23} and the presence of a Weyl node near the edge of conduction band.^{21,24–26} The nontrivial π Berry phase of Weyl fermions in the quantum oscillation sequence is reported in our previous work.²⁷

Te material usually manifests p-type behavior. A p-type accumulation layer^{28,29} at the crystal surface emerges since its chemical potential is aligned near the valence band. Atomic layer deposition (ALD) treatment removes the native oxide on the top surface and the positive fixed charges in ALD oxide converts the underneath 2D Te from p-type to n-type.³⁰ Hence, we can study the topological properties of Te conduction band in a controlled fashion. The device structure of double-gated Te field-effect transistors (FETs) is shown in Figure 1b. Te flakes grown by hydrothermal method³¹ are transferred onto 90 nm SiO₂/Si substrate. Titanium (50 nm) ensures the ohmic electrical contact to n-type Te. Ninety nanometers of SiO₂ and 20 nm of Al₂O₃, grown by ALD at 200 °C, are used as the back and top gate dielectrics, respectively. The optical image in Figure 1c shows a standard double-gated Hall-bar Te FET with the crystal orientations (determined in previous work³¹) indicated by the black arrows. The thickness of the Te flake is 20 nm in this study. Transverse (*R_{xy}*) and

Received: April 29, 2021

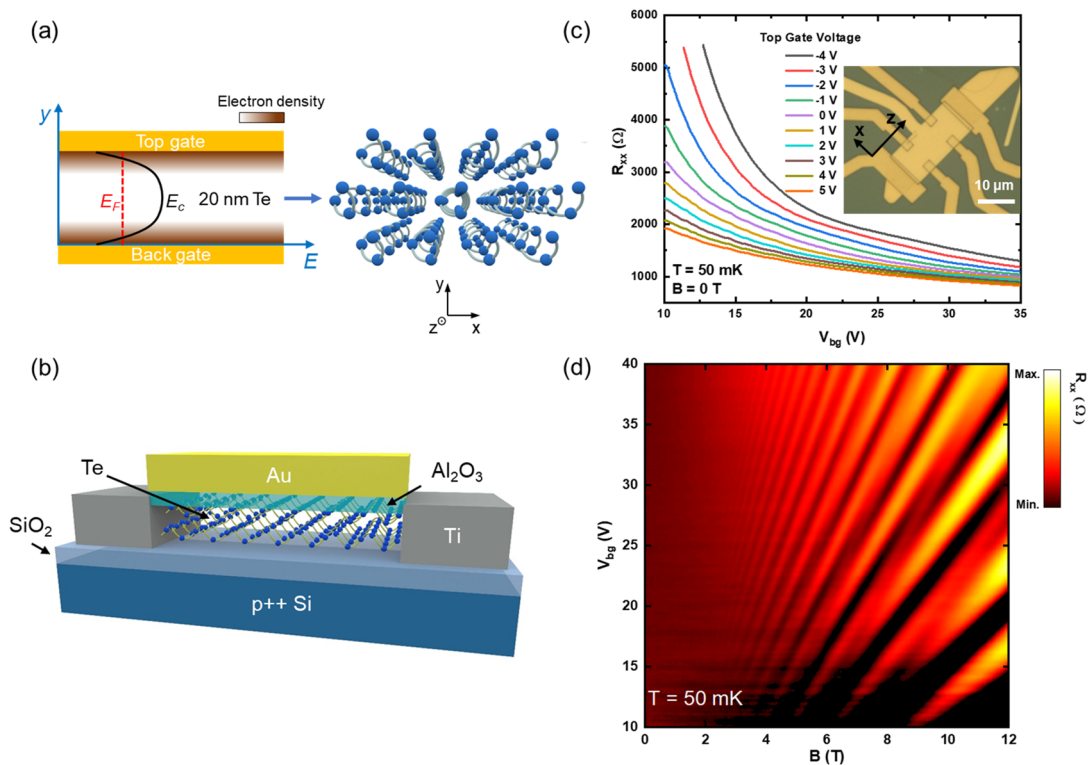


Figure 1. Structure and electrical transport of double-gated n-type 2D tellurium devices. (a) Band diagram of Te bilayer electron system and the crystal structure of Te. (b) The schematic device structure of Te field-effect transistor (FET) with 20 nm Al_2O_3 and 90 nm SiO_2 as gate dielectric. (c) Top and back gate voltage dependence of n-type Te channel resistance, measured at 50 mK. Inset: an optical image of double-gated Hall-bar 2D Te FET. (d) Color mapping of R_{xx} by sweeping both back gate voltage V_{bg} and magnetic field B at $V_{tg} = 0$ V.

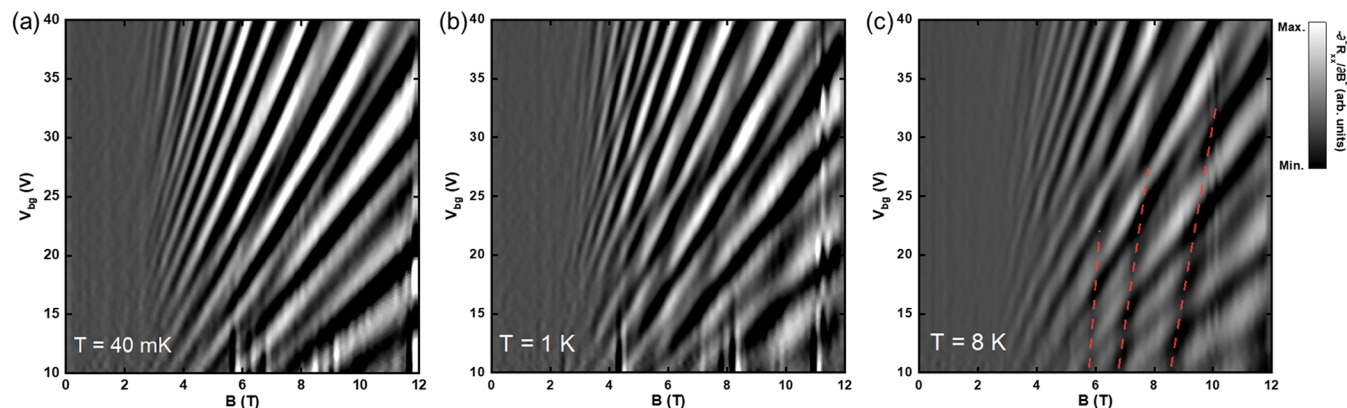


Figure 2. Color mapping of $-\partial^2 R_{xx}/\partial B^2$ by changing the back gate voltage V_{bg} and magnetic field B under various temperatures of 40 mK (a), 1 K (b), and 8 K (c). Top gate voltage V_{tg} is fixed at 0 V.

longitudinal (R_{xx}) resistance are measured at cryogenic temperature by inducing a current along the Te chain direction z .

In this paper, we systematically study the quantum transport of the bilayer electron system in an n-type 2D Te wide quantum well described above. Temperature and electron density dependence of quantum oscillations are measured in the magnetic field up to 31 T. Landau level hybridization between two layers and well-developed charge-transferable and compound states quantum Hall plateaus of filling factor $\nu = 4, 6, \text{ and } 8$ are observed.

RESULTS AND DISCUSSION

Top gate voltage V_{tg} and back gate voltage V_{bg} dependence of the Te channel resistance R_{xx} at cryogenic temperatures without magnetic field shown in Figure 1c confirms the n-type behavior of the double-gated Te device. Profound Shubnikov–de Haas (SdH) oscillations are observed when the magnetic field is applied perpendicular to the sample surface due to the high electron mobility of the 2D Te. By sweeping the back gate voltage V_{bg} (thus the carrier density) and the magnetic field B , a color mapping of R_{xx} can be measured, as shown in Figure 1d. Different Landau levels controlled by back gate voltage V_{bg} are identified. We attribute the complicated oscillation pattern to spin and valley splitting²¹ of the Te conduction band within a single layer of 2DEG.

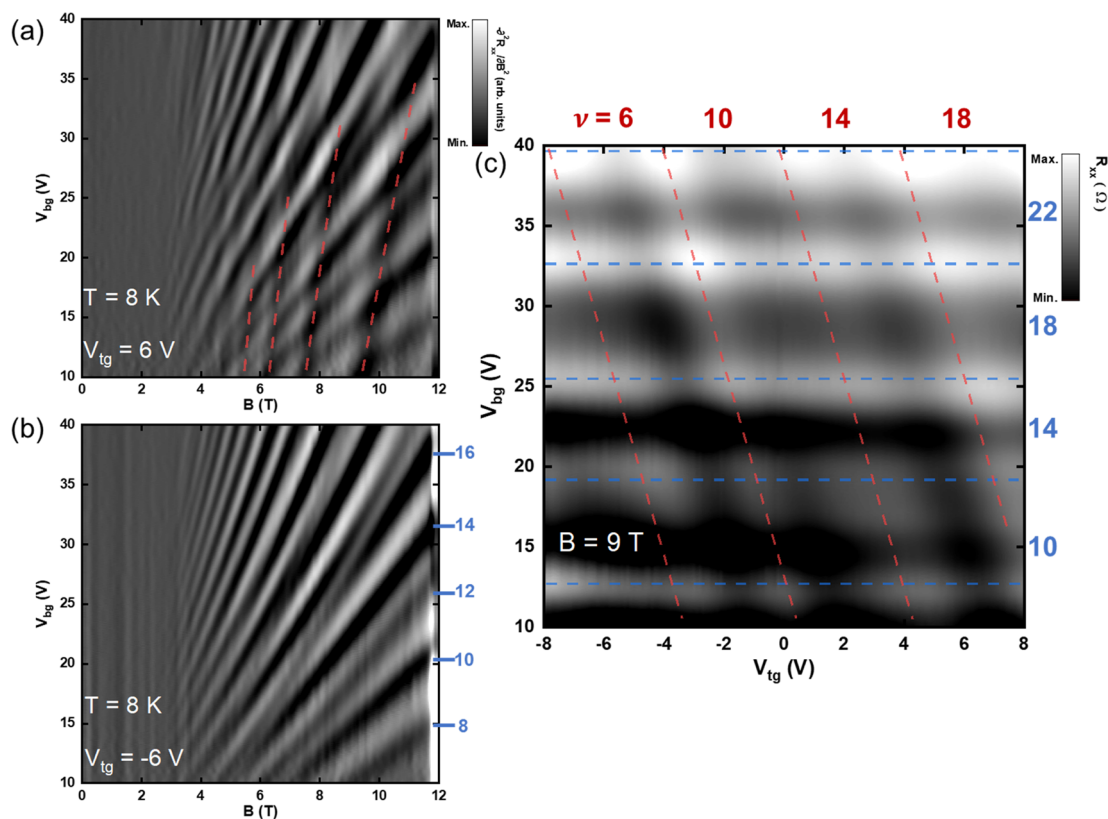


Figure 3. Bilayer quantum oscillations at $T = 8$ K. Color mapping of $-\partial^2 R_{xx}/\partial B^2$ by changing the back gate voltage V_{bg} and magnetic field B at $V_{tg} = 6$ V (a) and -6 V (b). Quantum oscillations (red dash lines) can be tuned by the top gate voltage V_{tg} , indicating that the oscillations originate from the top layer 2DEG. (c) Color mapping of R_{xx} by sweeping both V_{tg} and V_{bg} at $B = 9$ T. Two sets of Landau levels from the top (red dash lines) and bottom (blue dash lines) 2DEG controlled independently by V_{tg} and V_{bg} are observed.

To increase the resolution and visibility of the oscillation features, we take the second derivative of R_{xx} with respect to the magnetic field B . The mapping of $-\partial^2 R_{xx}/\partial B^2$ gives the same information with more clarity compared to the original data (R_{xx}), as shown in Figure S1. Figure 2 shows the temperature-dependent mapping of $-\partial^2 R_{xx}/\partial B^2$ from 40 mK to 8 K at $V_{tg} = 0$ V. Because of the ALD treatment at Te top surface, electrons in the top layer experience stronger surface scattering than bottom layer electrons. Therefore, the electron mobility of the top layer is relatively low. With the increase of temperature from 40 mK (Figure 2a) to 1 K (Figure 2b), the bottom layer electron mobility drops fast, and when it is comparable with the electron mobility of the top layer, another set of quantum oscillations from the top surface appears, indicated by the red eye guidelines in Figure 2c. Landau levels from different layers cross and form local maximum resistance points which is the bright area in the color mapping. We notice the small change of the Landau level crossing pattern at higher filling factors. This can also be explained by the Landau level hybridization between top and bottom layer 2DEGs (see Supporting Information Figure S2).

The SdH oscillations from top layer 2DEG can be tuned by changing the top gate voltage V_{tg} . Top layer carrier density is calculated from B_F (the SdH oscillation frequency in $1/B$) through $n = 4eB_F/h$ (here h is the Planck constant) with two-fold spin and two-fold valley degeneracies.³² The frequency of top layer 2DEG SdH oscillations (red dashed lines, Figure 3a) at $V_{tg} = 6$ V and $V_{bg} = 15$ V is 35 T, indicating a top layer carrier density of $n_t = 3.4 \times 10^{12}$ cm⁻². The system returns to single bottom quantum well dominant behavior with $V_{tg} = -6$

V (Figure 3b) due to the relatively low mobility and density of the top layer electrons. Figure 3c shows the top and back gate voltage dependence of the SdH oscillations at $B = 9$ T. Two sets of SdH oscillations controlled separately by V_{tg} and V_{bg} form a discrete spectrum with Landau level crossing at each lattice point, which is the signature of bilayer electron system transport.^{1,33} The top gate voltage V_{tg} does not influence the bottom layer quantum oscillations (blue dash lines) because of the charge screening from top layer electrons. On the other hand, the top layer electron density can be modulated by the back gate voltage V_{bg} . As the back gate voltage V_{bg} increases, the top layer electron density also increases, causing the Landau level shift in Figure 3a,c. The magnetic field B dependence of bilayer quantum oscillations can be seen in Figure S3 in the Supporting Information.

To further investigate the top layer quantum oscillations in double-gated Te FETs, we measured the color mapping of R_{xx} (Figure 4a) by sweeping top gate voltage V_{tg} and magnetic field B . SdH oscillations from bottom and top layer 2DEGs are separated when taking the second derivative of R_{xx} with respect to the magnetic field B ($-\partial^2 R_{xx}/\partial B^2$, Figure 4b) and the top gate voltage V_{tg} ($-\partial^2 R_{xx}/\partial V_{tg}^2$, Figure 4c). Vertical bright lines in Figure 4b show that the domination of the quantum oscillations originated from the bottom layer at $V_{bg} = 15$ V. By eliminating the bottom layer contribution, Landau levels controlled by top gate voltage are shown in Figure 4c. The lowest top surface Landau level we identified is $n = 2$ at the magnetic field of 12 T. Two gray curves in Figure 4b,c are R_{xx} at $V_{tg} = 0$ V and $-\partial^2 R_{xx}/\partial V_{tg}^2$ at $V_{tg} = 3.1$ V respectively. The same oscillation frequency between two curves indicates the

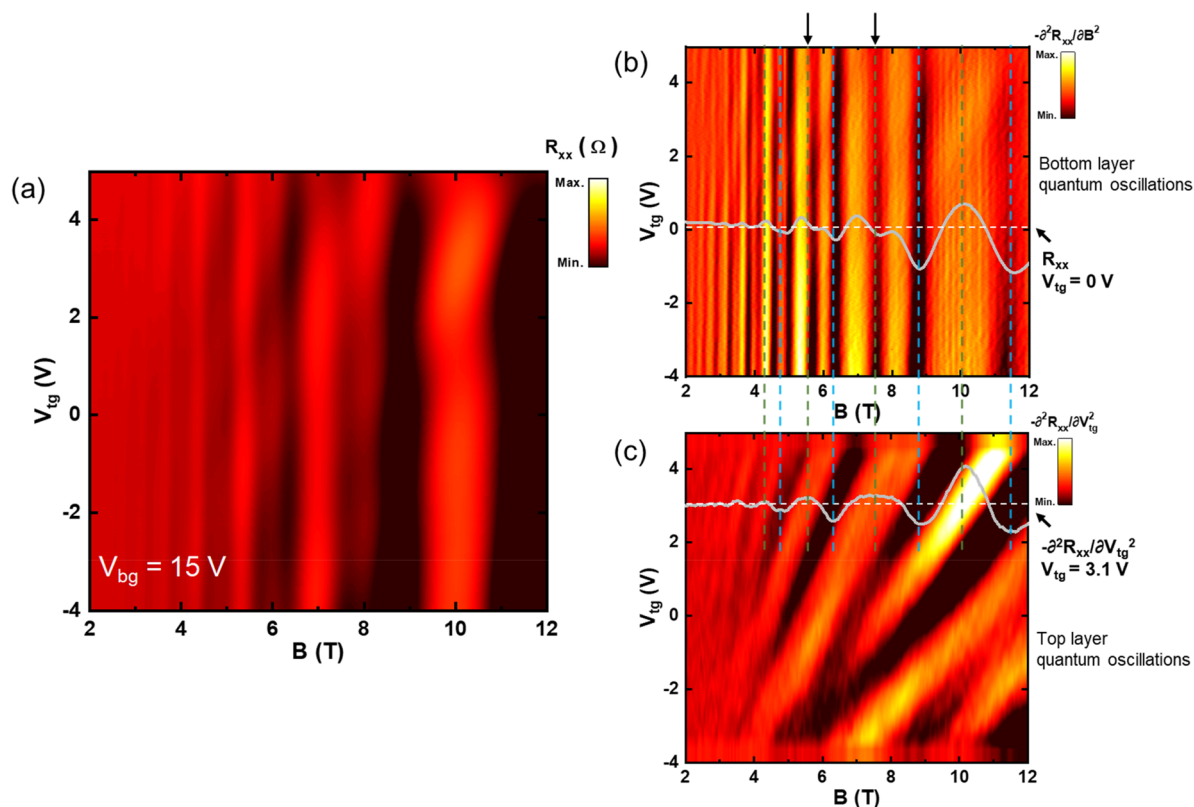


Figure 4. Color mapping of R_{xx} (a), $-\partial^2 R_{xx}/\partial B^2$ (b), and $-\partial^2 R_{xx}/\partial V_{tg}^2$ (c) by sweeping the top gate voltage V_{tg} and magnetic field B at $V_{bg} = 15$ V. The temperature is 50 mK. (b) Quantum oscillations from bottom layer 2DEG. The gray curve is R_{xx} data at $V_{tg} = 0$ V. (c) Quantum oscillations from top layer 2DEG. The gray curve is $-\partial^2 R_{xx}/\partial V_{tg}^2$ data at $V_{tg} = 3.1$ V. The green and blue eye guidelines are peak and dip positions of top layer SdH oscillations at $V_{tg} = 3.1$ V.

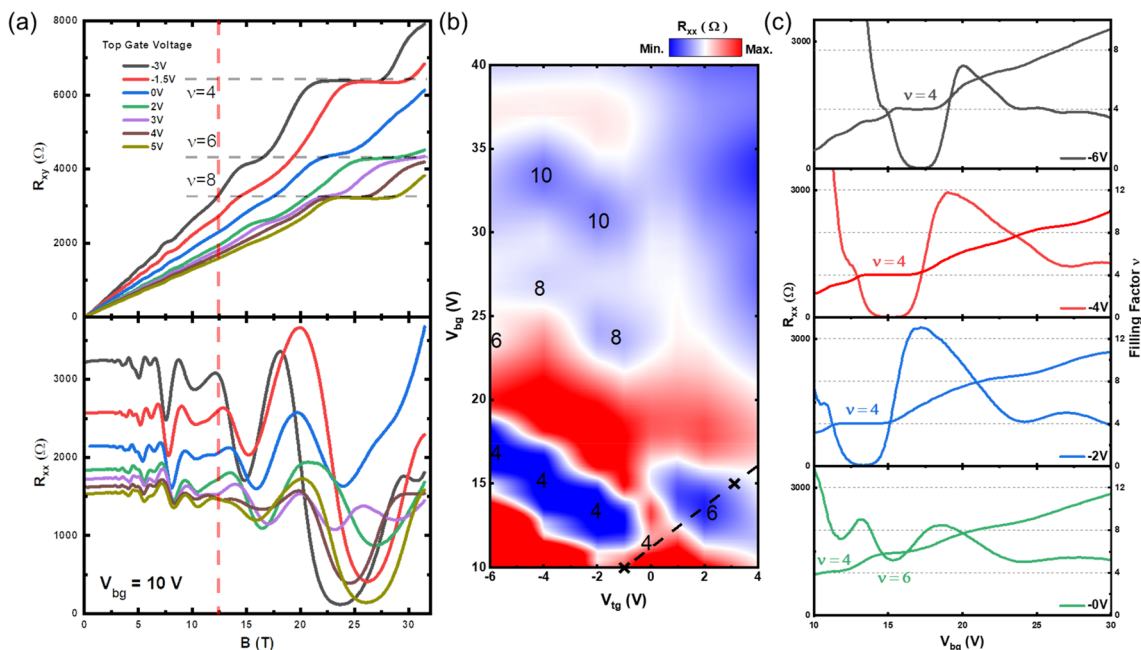


Figure 5. Compound and charge-transferable states in double-gated n-type 2D Te FETs. The temperature is 300 mK. (a) Transverse (R_{xy} , upper figure) and longitudinal (R_{xx} , lower figure) resistance as a function of magnetic field B . The back gate voltage is fixed at 15 V. Bilayer quantum Hall states are observed at filling factor $\nu = 4, 6$, and 8. (b) Color mapping of R_{xx} by changing both top and back gate voltage at the magnetic field of 31 T. The filling factor of each quantum Hall state is indicated in the color mapping. The top and bottom charges are balanced along the dashed line. (c) Longitudinal resistance (R_{xx}) as a function of back gate voltage at the magnetic field of 31 T by changing the top gate voltage from -6 to 0 V.

carrier density is balanced at two surfaces. The Landau level splitting (black arrows in Figure 4b) is not clear in top layer

SdH oscillation, because of the large Landau level broadening at the top surface. Complete measurement of the top layer

Landau fan diagram at different back gate voltage V_{bg} is shown in Supporting Information Figure S5. Landau level sequences in top and bottom layer 2DEG are identical.

A bilayer electron system provides an additional “which-layer” degree of freedom in the third direction and gives rise to various bilayer quantum Hall states. In analogue to the spin property of electrons, the SU(2) pseudospin ($P = P_x, P_y, P_z$) structure is used to describe the bilayer quantum Hall system.¹ Here the up-pseudospin ($P_z = 1/2$) component is the top-layer component and the down-pseudospin ($P_z = -1/2$) component is the bottom-layer component. The electron transfer between two layers is a rotation of the pseudospin. When the tunneling interaction between two layers is large, one Landau level splits into symmetric and antisymmetric states separated by the tunneling gap Δ_{SAS} . Charge-transferable states are realized when each level is filled. If $\Delta_{SAS} = 0$ (no electron tunneling), the pseudospin contains only the z -component. Compound states are observed at filling factor $\nu = \nu^t + \nu^b$, where ν^t (ν^b) is the filling factor of top (bottom) layer quantum Hall states.³⁴

Both compound and charge-transferable bilayer quantum Hall states of double-gated 2D n -type Te FETs are observed at low Landau levels shown in Figure 5, when a higher magnetic field is applied. Top gate voltage V_{tg} dependence of transverse (R_{xy} , Figure 5a upper figure) and longitudinal (R_{xx} , Figure 5a lower figure) resistance as a function of magnetic field B are measured at $V_{bg} = 10$ V. At a low magnetic field (below the red dash line), the frequency of the SdH oscillations that originated from the bottom layer 2DEG remains the same ($B_F = 15$ T) at different top gate voltages, indicating a fixed bottom layer electron density ($n_b = 1.5 \times 10^{12}$ cm⁻²) less sensitive to V_{tg} . However, at a high magnetic field well-developed quantum Hall plateaus of filling factor $\nu = 4, 6,$ and 8 are observed by increasing the V_{tg} (thus top layer electron density). Therefore, we conclude that quantum Hall states at filling factor 6 and 8 are compound states provided by both top and bottom layer 2DEG. The slight shift of the SdH oscillation minima and the change of the oscillation amplitude at lower magnetic field B indicate that the top gate has a small influence on the bottom layer electrons. The total electron density of the system determined by Hall measurement (Figure S6) linearly changes from 2.3×10^{12} cm⁻² ($V_{tg} = -3$ V) to 4.8×10^{12} cm⁻² ($V_{tg} = 5$ V). By comparing the total electron density and bottom layer quantum oscillation density, a carrier density balanced condition ($V_{bg} = 10$ V, $V_{tg} = -1$ V) is found between two 2DEGs. Figure 5b shows a color mapping of R_{xx} by changing V_{bg} and V_{tg} at a magnetic field of 31 T. The number in the color mapping represents the filling factor of the quantum Hall states. Carrier density balanced condition between two 2DEGs (black dash line) is obtained by connecting two carrier density balanced point (black crosses: $V_{bg} = 10$ V, $V_{tg} = -1$ V; $V_{bg} = 15$ V, $V_{tg} = 3.1$ V). We identify two compound states (ν^t, ν^b) at filling factor $\nu = 4$ ($2, 2$) and 6 ($3, 3$) along the carrier density balanced line in Figure 5b. Quantum Hall states are observed not only on a discrete lattice point (ν^t, ν^b) but also on elongated areas.³⁴ Instead of two independent single-layer quantum Hall states, the electrons in different layers at charge-transferable states are strongly correlated. The continuous quantum Hall states of filling factor 4 (from $V_{tg} = -6$ to 0 V) in Figure 5b,c indicate the charge is transferable between top and bottom layer 2DEG. The wave functions of electrons in the top and bottom layers overlap when the gate bias is relatively low, giving rise to a finite tunneling gap Δ_{SAS} . The charge transferable states can be

observed in higher filling factors $\nu = 6, 8, 10,$ and 12 at the magnetic field of 12 T in another 20 nm-thick 2D Te FET with two 2DEG layers (see Supporting Information Figures S7 and S8), indicating a complicated Landau level hybridization between top and bottom layer 2DEG. Because of the Weyl node at the edge of the conduction band,²¹ the quantum oscillations of the Weyl Fermions show a topological nontrivial π -phase shift.²⁷ In Figure S9, we extracted the Landau fan diagram of the top and bottom layer 2DEG by assigning the integer Landau level index n to the minima in quantum oscillations. The 0.5 intercept indicates the presence of the Weyl Fermions in both top and bottom layers. Further improved device fabrication and clearer quantum oscillation features would provide a new interesting platform to investigate the correlated bilayer Weyl Fermions and explore new topological physics.

CONCLUSION

In conclusion, double-gated n -type 2D Te FETs were fabricated and measured. SdH oscillations from the top and bottom layer 2DEG controlled by the top and back gates are observed and separated. With the presence of an additional “which-layer” degree of freedom, the Landau level hybridization between top and bottom layer 2DEGs is studied. Compound and charge-transferable bilayer quantum Hall states of filling factor $\nu = 4, 6,$ and 8 are identified in a wide Te quantum well structure at a high magnetic field. The realization of two well-controlled high mobility 2DEGs in an n -type wide Te quantum well provides an ideal platform for the study of the Weyl physics in bilayer systems.

METHODS

Growth of 2D Te Flake. The 2D Te flakes are grown by hydrothermal method. A sample of 0.09 g of Na_2TeO_3 and 0.5 g of polyvinylpyrrolidone (PVP) (Sigma-Aldrich) were dissolved in 33 mL of double-distilled water under magnetic stirring to form a homogeneous solution. A sample of 3.33 mL of aqueous ammonia solution (25 – 28% , w/w%) and 1.67 mL of hydrazine hydrate (80% , w/w%) were added to the solution. The mixture was sealed in a 50 mL Teflon-lined stainless steel autoclave and heated at 180 °C for 30 h before naturally cooling down to room temperature.

Device Fabrication. Te flakes were transferred onto 90 nm SiO_2/Si substrate. The six-terminal Hall-bar devices were patterned using two step electron beam lithography, and 50 nm Ti, $20/60$ nm Ti/Au metal contacts were deposited by electron beam evaporation. Twenty nm ALD Al_2O_3 which served as top gate dielectric was deposited onto the Te flakes at 200 °C using $(\text{CH}_3)_3\text{Al}$ (TMA) and H_2O as precursors. The top gate metal (50 nm Au) was deposited using electron beam evaporation after electron beam lithography patterning.

Low-Temperature Magneto-Transport Measurements. The magneto-transport measurements were performed in a Triton 300 (Oxford Instruments) dilution fridge system with 12 T superconducting coils at temperatures down to 50 mK. The high magnetic-field data were collected in a 31 T resistive magnet system (Cell 9) at the National High Magnetic Field Laboratory (NHMFL) in Tallahassee, FL. The electrical data were acquired by standard small signal AC measurement technique using SR830 lock-in amplifiers (Stanford Research) at the frequency of 13.333 Hz.

■ ASSOCIATED CONTENT

SI Supporting Information

The Supporting Information is available free of charge at <https://pubs.acs.org/doi/10.1021/acs.nanolett.1c01705>.

Additional details for mobility and carrier density, comparison between R_{xx} and $-\partial^2 R_{xx}/\partial B^2$, Landau level crossing at high filling factor, top gate dependence of Landau level mapping at 8 K, bilayer quantum oscillation at different magnetic field, back gate dependence of top layer Landau level mapping, and top gate dependence of total Hall density at $V_{bg} = 10$ V (PDF)

■ AUTHOR INFORMATION

Corresponding Author

Peide D. Ye – School of Electrical and Computer Engineering, Purdue University, West Lafayette, Indiana 47907, United States; Birck Nanotechnology Center, Purdue University, West Lafayette, Indiana 47907, United States; orcid.org/0000-0001-8466-9745; Email: yep@purdue.edu

Authors

Chang Niu – School of Electrical and Computer Engineering, Purdue University, West Lafayette, Indiana 47907, United States; Birck Nanotechnology Center, Purdue University, West Lafayette, Indiana 47907, United States; orcid.org/0000-0003-3175-7164

Gang Qiu – School of Electrical and Computer Engineering, Purdue University, West Lafayette, Indiana 47907, United States; Birck Nanotechnology Center, Purdue University, West Lafayette, Indiana 47907, United States

Yixiu Wang – School of Industrial Engineering, Purdue University, West Lafayette, Indiana 47907, United States

Mengwei Si – School of Electrical and Computer Engineering, Purdue University, West Lafayette, Indiana 47907, United States; Birck Nanotechnology Center, Purdue University, West Lafayette, Indiana 47907, United States; orcid.org/0000-0003-0397-7741

Wenzhuo Wu – School of Industrial Engineering, Purdue University, West Lafayette, Indiana 47907, United States; orcid.org/0000-0003-0362-6650

Complete contact information is available at: <https://pubs.acs.org/doi/10.1021/acs.nanolett.1c01705>

Author Contributions

P.D.Y. conceived and supervised the project. P.D.Y. and C.N. designed the experiments. Y.W. synthesized the material under the supervision of W.W. C.N. and G.Q. fabricated the devices. C.N. and G.Q. performed the magneto-transport measurements. C.N., G.Q., and M.S. analyzed the data. P.D.Y. and C.N. wrote the manuscript and all the authors commented on it.

Notes

The authors declare no competing financial interest.

■ ACKNOWLEDGMENTS

P.D.Y. was supported by NSF/AFOSR 2DARE program, ARO and SRC. W.W. acknowledges the School of Industrial Engineering at Purdue University for the Ravi and Eleanor Talwar Rising Star Professorship support. W.W. and P.D.Y. were also supported by NSF under Grant CMMI-1762698. A portion of this work was performed at the National High Magnetic Field Laboratory, which is supported by National

Science Foundation Cooperative Agreement No. DMR-1644779 and the State of Florida. C.N. and G.Q. acknowledge technical support from National High Magnetic Field Laboratory Staff J. Jaroszynski, A. Suslov, and W. Coniglio.

■ REFERENCES

- (1) Ezawa, Z. F. *Quantum Hall Effects: Recent theoretical and experimental developments*; World Scientific Publishing Company: Singapore, 2013.
- (2) Suen, Y. W.; Santos, M. B.; Shayegan, M. Correlated States of an Electron System in a Wide Quantum Well. *Phys. Rev. Lett.* **1992**, *69* (24), 3551–3554.
- (3) Li, J. I. A.; Shi, Q.; Zeng, Y.; Watanabe, K.; Taniguchi, T.; Hone, J.; Dean, C. R. Pairing States of Composite Fermions in Double-Layer Graphene. *Nat. Phys.* **2019**, *15* (9), 898–903.
- (4) Suen, Y. W.; Engel, L. W.; Santos, M. B.; Shayegan, M.; Tsui, D. C. Observation of a $\nu = 1/2$ Fractional Quantum Hall State in a Double-Layer Electron System. *Phys. Rev. Lett.* **1992**, *68* (9), 1379–1382.
- (5) Murphy, S. Q.; Eisenstein, J. P.; Boebinger, G. S.; Pfeiffer, L. N.; West, K. W. Many-Body Integer Quantum Hall Effect: Evidence for New Phase Transitions. *Phys. Rev. Lett.* **1994**, *72* (5), 728–731.
- (6) Sawada, A.; Ezawa, Z. F.; Ohno, H.; Horikoshi, Y.; Ohno, Y.; Kishimoto, S.; Matsukura, F.; Yasumoto, M.; Urayama, A. Phase Transition in the $N = 2$ Bilayer Quantum Hall State. *Phys. Rev. Lett.* **1998**, *80* (20), 4534–4537.
- (7) Eisenstein, J. P.; Boebinger, G. S.; Pfeiffer, L. N.; West, K. W.; He, S. New Fractional Quantum Hall State in Double-Layer Two-Dimensional Electron Systems. *Phys. Rev. Lett.* **1992**, *68* (9), 1383–1386.
- (8) Spielman, I. B.; Eisenstein, J. P.; Pfeiffer, L. N.; West, K. W. Resonantly Enhanced Tunneling in a Double Layer Quantum Hall Ferromagnet. *Phys. Rev. Lett.* **2000**, *84* (25), 5808–5811.
- (9) Liu, X.; Watanabe, K.; Taniguchi, T.; Halperin, B. I.; Kim, P. Quantum Hall Drag of Exciton Condensate in Graphene. *Nat. Phys.* **2017**, *13* (8), 746–750.
- (10) Kim, S.; Jo, I.; Nah, J.; Yao, Z.; Banerjee, S. K.; Tutuc, E. Coulomb Drag of Massless Fermions in Graphene. *Phys. Rev. B: Condens. Matter Mater. Phys.* **2011**, *83* (16), 161401.
- (11) Ezawa, Z. F.; Iwazaki, A. Quantum Hall Liquid, Josephson Effect, and Hierarchy in a Double-Layer Electron System. *Phys. Rev. B: Condens. Matter Mater. Phys.* **1993**, *47* (12), 7295–7311.
- (12) Li, J. I. A.; Taniguchi, T.; Watanabe, K.; Hone, J.; Dean, C. R. Excitonic Superfluid Phase in Double Bilayer Graphene. *Nat. Phys.* **2017**, *13* (8), 751–755.
- (13) Eisenstein, J. P.; MacDonald, A. H. Bose–Einstein Condensation of Excitons in Bilayer Electron Systems. *Nature* **2004**, *432*, 691–694.
- (14) Rasolt, M.; MacDonald, A. H. Collective Excitations in the Fractional Quantum Hall Effect of a Multicomponent Fermion System. *Phys. Rev. B: Condens. Matter Mater. Phys.* **1986**, *34* (8), 5530–5539.
- (15) Boebinger, G. S.; Jiang, H. W.; Pfeiffer, L. N.; West, K. W. Magnetic-Field-Driven Destruction of Quantum Hall States in a Double Quantum Well. *Phys. Rev. Lett.* **1990**, *64* (15), 1793–1796.
- (16) Suen, Y. W.; Jo, J.; Santos, M. B.; Engel, L. W.; Hwang, S. W.; Shayegan, M. Missing Integral Quantum Hall Effect in a Wide Single Quantum Well. *Phys. Rev. B: Condens. Matter Mater. Phys.* **1991**, *44* (11), 5947–5950.
- (17) Shinno, H.; Yoshizaki, R.; Tanaka, S.; Doi, T.; Kamimura, H. Conduction Band Structure of Tellurium. *J. Phys. Soc. Jpn.* **1973**, *35* (2), 525–533.
- (18) Niu, C.; Qiu, G.; Wang, Y.; Zhang, Z.; Si, M.; Wu, W.; Ye, P. D. Gate-Tunable Strong Spin-Orbit Interaction in Two-Dimensional Tellurium Probed by Weak Antilocalization. *Phys. Rev. B: Condens. Matter Mater. Phys.* **2020**, *101* (20), 205414.

- (19) Doi, T.; Nakao, K.; Kamimura, H. The Valence Band Structure of Tellurium. I. The K-p Perturbation Method. *J. Phys. Soc. Jpn.* **1970**, *28* (1), 36–43.
- (20) Ando, T. Theory of Magnetoresistance in Tellurene and Related Mini-Gap Systems. *J. Phys. Soc. Jpn.* **2021**, *90* (4), 044711.
- (21) Hirayama, M.; Okugawa, R.; Ishibashi, S.; Murakami, S.; Miyake, T. Weyl Node and Spin Texture in Trigonal Tellurium and Selenium. *Phys. Rev. Lett.* **2015**, *114* (20), 206401.
- (22) Sakano, M.; Hirayama, M.; Takahashi, T.; Akebi, S.; Nakayama, M.; Kuroda, K.; Taguchi, K.; Yoshikawa, T.; Miyamoto, K.; Okuda, T.; et al. Radial Spin Texture in Elemental Tellurium with Chiral Crystal Structure. *Phys. Rev. Lett.* **2020**, *124* (13), 136404.
- (23) Gatti, G.; Gosálbez-Martínez, D.; Tsirkin, S. S.; Fanciulli, M.; Puppini, M.; Polishchuk, S.; Moser, S.; Testa, L.; Martino, E.; Roth, S.; et al. Radial Spin Texture of the Weyl Fermions in Chiral Tellurium. *Phys. Rev. Lett.* **2020**, *125* (21), 216402.
- (24) Agapito, L. A.; Kioussis, N.; Goddard, W. A.; Ong, N. P. Novel Family of Chiral-Based Topological Insulators: Elemental Tellurium under Strain. *Phys. Rev. Lett.* **2013**, *110* (17), 176401.
- (25) Tsirkin, S. S.; Puente, P. A.; Souza, I. Gyrotropic Effects in Trigonal Tellurium Studied from First Principles. *Phys. Rev. B: Condens. Matter Mater. Phys.* **2018**, *97* (3), 035158.
- (26) Şahin, C.; Rou, J.; Ma, J.; Pesin, D. A. Pancharatnam-Berry Phase and Kinetic Magnetoelectric Effect in Trigonal Tellurium. *Phys. Rev. B: Condens. Matter Mater. Phys.* **2018**, *97* (20), 205206.
- (27) Qiu, G.; Niu, C.; Wang, Y.; Si, M.; Zhang, Z.; Wu, W.; Ye, P. D. Quantum Hall Effect of Weyl Fermions in N-Type Semiconducting Tellurene. *Nat. Nanotechnol.* **2020**, *15* (7), 585–591.
- (28) Berezovets, V. A.; Farbshtein, I. I.; Shelankov, A. L. Weak Localization under Lifted Spin-Degeneracy Conditions (Two-Dimensional Layer on a Tellurium Surface). *JETP Lett.* **1984**, *39*, 64.
- (29) Akiba, K.; Kobayashi, K.; Kobayashi, T. C.; Koezuka, R.; Miyake, A.; Gouchi, J.; Uwatoko, Y.; Tokunaga, M. Magnetotransport Properties of Tellurium under Extreme Conditions. *Phys. Rev. B: Condens. Matter Mater. Phys.* **2020**, *101*, 245111.
- (30) Qiu, G.; Si, M.; Wang, Y.; Lyu, X.; Wu, W.; Ye, P. D. High-Performance Few-Layer Tellurium CMOS Devices Enabled by Atomic Layer Deposited Dielectric Doping Technique. *Device Research Conference (DRC)* 2018.
- (31) Wang, Y.; Qiu, G.; Wang, R.; Huang, S.; Wang, Q.; Liu, Y.; Du, Y.; Goddard, W. A.; Kim, M. J.; Xu, X.; et al. Field-Effect Transistors Made from Solution-Grown Two-Dimensional Tellurene. *Nat. Electron.* **2018**, *1* (4), 228–236.
- (32) Datta, S. *Electronic Transport in Mesoscopic Systems*; Cambridge University Press: Cambridge, United Kingdom, 1997.
- (33) Tran, S.; Yang, J.; Gillgren, N.; Espiritu, T.; Shi, Y.; Watanabe, K.; Taniguchi, T.; Moon, S.; Baek, H.; Smirnov, D.; Bockrath, M.; Chen, R.; Lau, C. N. Surface transport and quantum Hall effect in ambipolar black phosphorus double quantum wells. *Science Advances* **2017**, *3* (6), 1603179.
- (34) Muraki, K.; Saku, T.; Hirayama, Y.; Kumada, N.; Sawada, A.; Ezawa, Z. F. Interlayer Charge Transfer in Bilayer Quantum Hall States at Various Filling Factors. *Solid State Commun.* **1999**, *112* (11), 625–629.